BIOPHYSICS

In situ measurements of intracellular thermal conductivity using heater-thermometer hybrid diamond nanosensors

Shingo Sotoma[1,2]*, Chongxia Zhong[1]*, James Chen Yong Kah[3], Hayato Yamashita[4,5], Taras Plakhotnik[6]†, Yoshie Harada[1,7]†, Madoka Suzuki[1,5]†

Understanding heat dissipation processes at nanoscale during cellular thermogenesis is essential to clarify the relationships between the heat and biological processes in cells and organisms. A key parameter determining the heat flux inside a cell is the local thermal conductivity, a factor poorly investigated both experimentally and theoretically. Here, using a nanoheater/nanothermometer hybrid made of a polydopamine encapsulating a fluorescent nanodiamond, we measured the intracellular thermal conductivities of HeLa and MCF-7 cells with a spatial resolution of about 200 nm. The mean values determined in these two cell lines are both 0.11 ± 0.04 W m^{-1} K^{-1}, which is significantly smaller than that of water. Bayesian analysis of the data suggests there is a variation of the thermal conductivity within a cell. These results make the biological impact of transient temperature spikes in a cell much more feasible, and suggest that cells may use heat flux for short-distance thermal signaling.

INTRODUCTION

Internal heat, a distinctive feature of mammals and birds, was possibly developed in dinosaurs (*1*) but also occurs in extant plants (*2*, *3*) and fishes (*4*). Investigation of heat in insects has begun centuries ago (*5*). Despite the long history, understanding of heat generation and control in organisms and cells is still incomplete. The heat originates from intracellular biochemical sources and then flows through cells to elevate the temperature of the whole body. The body temperature, in turn, is a factor governing enzymatic activities including those of heat sources (*6*). Thus, simultaneous observation of biochemical processes at the heat source and the dynamics of heat flow in situ is essential for developing a realistic model of heat release and management in living organisms.

Luminescence nanothermometry is a tool suitable for achieving this ambitious goal, because it enables visualization of temperature changes in cells with subcellular resolution (*7*, *8*). Several groups used this tool and have recently reported temperature heterogeneity over 1 K in individual cells (*9*–*12*). These reports have prompted active discussions about the origin and the biological significance of the heterogeneity. However, the results have also sparked hot debates about the validity of the temperature measurements (*13*–*18*). The issue is that the temperature rise calculated by theoretical models describing physics of cellular thermogenesis and intracellular space is several orders of magnitude smaller than the experimental values reported in the literature. One of the essential factors in the calculation is the thermal conductivity, a parameter determining heat flux and which is usually assumed to be approximately 0.6 W m^{-1} K^{-1}, similar to that found in watery environments. However, Bastos *et al.* (*19*) have used upconverting nanoparticles to measure the thermal conductivity of a single lipid bilayer and reported a value of 0.2 W m^{-1} K^{-1}. When the boundary heat resistance is considered theoretically (*18*), the estimated thermal conductivity in cells is smaller than in water by a factor of 6. Although experimentally determining the thermal conductivity in living cells and assessing its variation at nanoscale levels is critical, no such information is currently available, to the best of our knowledge.

A two-in-one nanodevice that provides heating and temperature sensing at the same time and the same spot is a straightforward strategy for measuring intracellular thermal conductivity locally. Tsai *et al.* (*20*, *21*) have reported the use of fluorescent nanodiamond (FND) and gold nanorods (GNRs). FNDs containing negatively charged nitrogen-vacancy centers (NVCs) are known as a fluorescent nanomaterial, showing neither photobleaching nor photoblinking (*22*, *23*). Physically bound FNDs and GNRs serve simultaneously as nanothermometers and nanoheaters, because the unique magneto-optical properties of NVCs in FNDs allow nanoscale temperature measurement (*24*–*26*) and GNRs release heat when exposed to light via their strong surface plasmon resonance (*27*). However, the stoichiometry of FND/GNR ratio is difficult to control, and GNRs can be deformed by heating, which makes quantitative and reproducible experiments difficult.

Here, we propose FND and polydopamine (PDA) nanohybrids (PDA-FNDs) to overcome these difficulties. Under basic conditions, dopamine molecules polymerize to form a PDA layer on the surface of inorganic materials. The PDA layer works as a platform for chemical functionalization (*28*–*31*). In addition, PDAs demonstrate high photothermal conversion efficiency; therefore, PDA-coated nanoparticles (e.g., gold, magnetic, and silica nanoparticles) have been used for multifunctional hyperthermia applications, especially for cancer therapy (*29*, *32*). We characterized the physical properties of PDA-FNDs, investigated how they affected the release of heat, and measured the thermal conductivity inside living single cells of two cell lines with submicrometer spatial resolution.

---

[1]Institute for Protein Research, Osaka University, Osaka, Japan. [2]Japan Society for the Promotion of Science, Tokyo, Japan. [3]Department of Biomedical Engineering, National University of Singapore, Singapore, Singapore. [4]Graduate School of Engineering Science, Osaka University, Osaka, Japan. [5]PRESTO, Japan Science and Technology Agency, Saitama, Japan. [6]School of Mathematics and Physics, The University of Queensland, QLD, Australia. [7]Quantum Information and Quantum Biology Division, Institute for Open and Transdisciplinary Research Initiatives, Osaka University, Osaka, Japan.
*These authors contributed equally to this work.
†Corresponding author. Email: taras@physics.uq.edu.au (T.P.); yharada@protein.osaka-u.ac.jp (Y.H.); suzu_mado@protein.osaka-u.ac.jp (M.S.)

RESULTS

Synthesis and characterization of PDA-FNDs

Dopamine molecules are polymerized into PDAs on the surface of FNDs in tris-HCl buffer (pH 8.5), thus yielding PDA-FNDs after centrifugation and washing (Fig. 1A). The size, shape, and thickness of the PDA layers were evaluated by transmission electron microscopy (TEM). TEM images showed that FNDs have sharp edges and wide distributions in size and shape (Fig. 1B). After PDA coating, PDA-FND particles had relatively smooth edges. The thickness of the PDA layers increased as the concentration of dopamine hydrochloride solutions increased (Fig. 1C). The thicknesses of the PDA layers appear to be constant regardless of the size of the FNDs (Fig. 1D). The mean hydrodynamic diameter and the zeta potentials of PDA-FNDs are shown in fig. S1.

Dual functionality of PDA-FND nanoparticles

PDA-FNDs are hybrids consisting of luminescent nanothermometers and optically controlled nanoheaters. The ground state of the negatively charged NV (NV^-) center in FNDs is a spin-triplet. The split of the spin sublevels, $m_s = 0$ and $m_s = \pm 1$ denoted as $D_{gs} \approx 2870$ MHz, is temperature dependent with a reported gradient (*24*, *25*) of $\gamma \approx -0.074$ MHz K^{-1} (fig. S2). Photoluminescence, excited at 532 nm, decreases when the transition from $m_s = 0$ to either the $m_s = +1$ or the $m_s = -1$ state occurs at resonance with applied external microwave (MW) radiation (Fig. 2A).

The values of D_{gs} vary from particle to particle in the range of 2869 to 2870 MHz at 0.95-mW excitation due to the inherent heterogeneity of FNDs (*33*, *34*), but D_{gs} decreases at higher laser powers as expected in the case of rising temperatures (fig. S3). Heterogeneity of D_{gs} prevents absolute measurements of temperature, but the temperature difference, $dT_{P1 \to P2}$, caused by the change of the excitation power from P_1 to P_2 can be obtained by monitoring the shift in D_{gs} values. The values of $dT_{P1 \to P2}$ are approximately four times larger for particles prepared using 500 µg/ml dopamine hydrochloride solution than for pristine FNDs (Fig. 2B and fig. S3). The PDA-FNDs prepared under 50 µg/ml dopamine hydrochloride solution showed

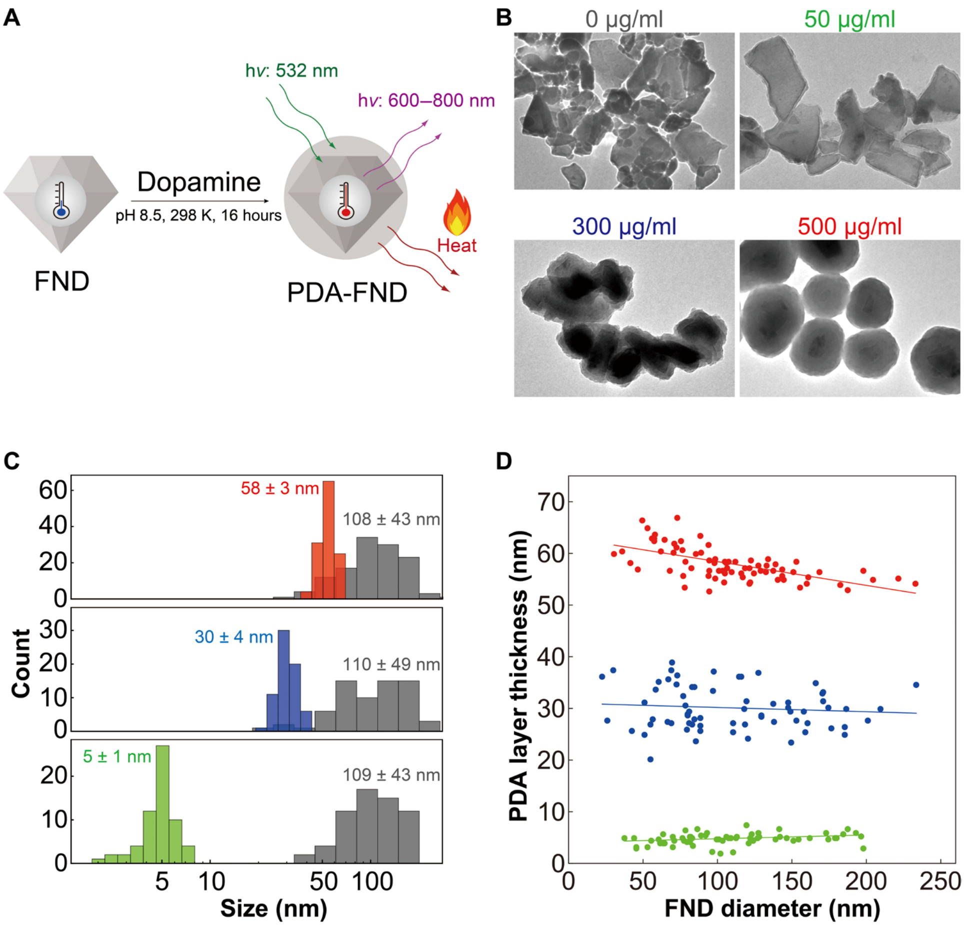

Fig. 1. Characterization of polydopamine and fluorescent nanodiamond hybrid particles (PDA-FNDs). (**A**) Schematic illustration of the dual-functionalized PDA-FNDs prepared from FNDs. The FND functions as a luminescent nanothermometer, while PDA releases heat in a light-dependent manner. (**B**) Representative transmission electron microscope (TEM) images of PDA-FNDs prepared with various concentrations of dopamine hydrochloride solutions as indicated above each image. Image size: 751 × 534 nm. Brightness and contrast were adjusted for viewing purposes. (**C**) Histograms of FND diameters (gray) and PDA layer thicknesses of PDA-FNDs prepared with dopamine hydrochloride solutions of 50 µg/ml (green), 300 µg/ml (blue), and 500 µg/ml (red) measured from the respective TEM images. The average thicknesses of the coating layers and the average diameters of FNDs with the respective SDs of the distributions are displayed in each panel. (**D**) The relationship between the FND diameters and the PDA layer thicknesses of PDA-FNDs prepared with dopamine hydrochloride solutions at concentrations of 50 µg/ml (green, $n = 62$ particles), 300 µg/ml (blue, $n = 68$ particles), or 500 µg/ml (red, $n = 75$ particles). The gradients of the straight lines are small (0.72, −0.83, and −4.6% for 50, 300, and 500 µg/ml samples, respectively).

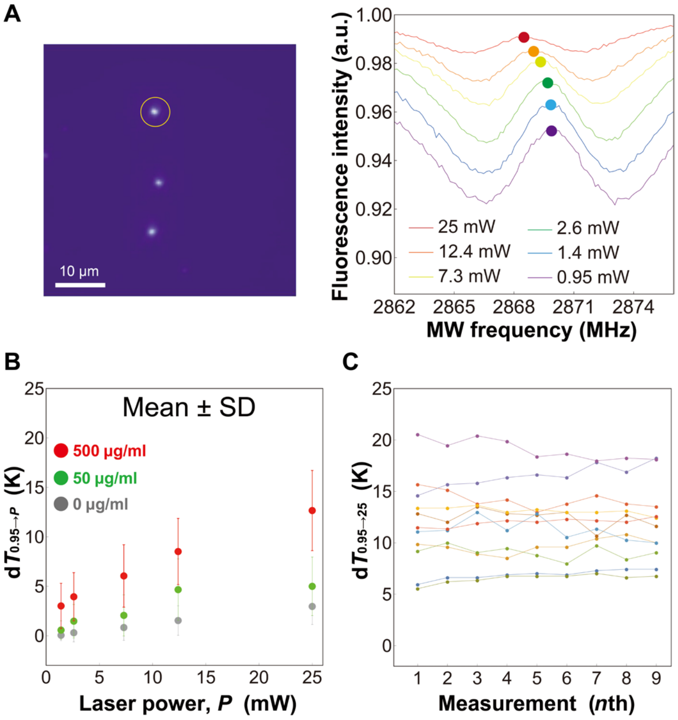

Fig. 2. Application of PDA-FNDs as individual nanoheater/nanothermometer composites. PDA-FNDs for which data are shown in (A) to (C) were prepared using dopamine chloride solution (500 μg/ml). In all cases, the nanocrystals are dispersed on a glass substrate in air. (**A**) Typical fluorescence image of PDA-FNDs on a coverslip and the optically detected magnetic resonance (ODMR) spectra over external microwave (MW) radiation recorded with different excitation laser powers. The ODMR spectra are of a PDA-FND indicated by the yellow circle in the image. The contrast of the ODMR signal decreases at larger excitation powers probably due to the photoinduced conversion of the negatively charged NVCs to ODMR-inactive neutral NVCs (*53*). a.u., arbitrary units. (**B**) Temperature change d$T_{0.95\to P}$ estimated from the change of D_{gs} in PDA-FND particles compared to pristine FNDs. The panel shows the corresponding mean values (circles) and the sample SDs (bars). (**C**) Values of d$T_{0.95\to 25}$ (the temperature change when the laser power changed from 0.95 to 25 mW) in 11 individual PDA-FNDs obtained in nine sequential measurements.

intermediate photothermal efficacy, implying that thin PDAs can serve as scaffolds for further functionalization with some precautions related to heating and additionally can safeguard some applications against undesirable heating of the functionalized material (*35*, *36*). PDA-FNDs, prepared from 500 μg/ml solutions, were used in subsequent experiments since they have large photothermal effects, yet do not substantially hinder FND fluorescence.

To assess the photostability of PDA, optically detected magnetic resonance (ODMR) was repeatedly measured for nine successive measurements of d$T_{0.95\to 25}$ using the same set of individual PDA-FNDs. The temperature rise remained nearly constant in the series (Fig. 2C and fig. S4). These results indicated that the PDA layer in PDA-FNDs remained stable after multiple excitations and that the heat release was reproducible under the current experimental conditions.

Cellular uptake and intracellular localization of PDA-FNDs

The biocompatibility, cellular uptake, and intracellular localization of PDA-FNDs were examined in HeLa cells. It has been reported that both FNDs (*37*, *38*) and PDA nanoparticles (*39*) are biocompatible with various types of cells. The results of the cell viability test indicated that PDA-FNDs only slightly affect the viability of HeLa cells (Fig. 3A). The concentration of PDA-FNDs used in the ODMR experiments was ≤1 μg/ml, approximately 15% of the lowest concentration in Fig. 3A.

PDA-FNDs were internalized by HeLa cells and became localized primarily at the perinuclear region after a 4-hour incubation according to confocal observations (Fig. 3B). FNDs are known to enter cells via adenosine 5′-triphosphate (ATP)–dependent endocytosis, which is commonly observed among particles up to 150 nm in diameter (*40*). To investigate the role of endocytosis in this case, we evaluated the effect of sodium azide (NaN_3), an inhibitor of F_0F_1 ATP synthase, on the cellular uptake of PDA-FNDs. Confocal microscopy results showed that the amount of PDA-FNDs internalized by HeLa cells decreased remarkably in NaN_3-treated cells compared to nontreated cells (fig. S5). Quantitative fluorescence-activated cell sorting (FACS) analysis further supported the microscopic observations (Fig. 3C). These results suggest that PDA-FND uptake in HeLa cells is through energy-dependent endocytosis.

Further investigation of the subcellular localization showed that most of the PDA-FNDs (453 of the total 526 particles in 53 cells) are present in lysosome-associated membrane protein 1 (LAMP1)–green fluorescent protein (GFP) (*41*)–positive vesicles (Fig. 3D). A small portion of PDA-FNDs (73 particles) in cells did not colocalize with LAMP1-GFP–positive vesicles and might be located either in LAMP1-GFP–negative vesicles or in the cytosol (fig. S5). Since the integrity of the PDA layer is preserved under acidic conditions in lysosomes (fig. S6), PDA-FNDs are suitable for intracellular measurements.

In situ measurements of intracellular thermal conductivity

The steady-state spatial temperature distribution $T(\vec{\mathbf{r}})$ follows Fourier's heat conduction equation

$$-\kappa \nabla^2 T = \dot{q} \tag{1}$$

where κ is the thermal conductivity of the media and $\dot{q}(r)$ is the heat power density. One can solve Eq. 1 to obtain $T(\vec{\mathbf{r}})$. The essential details of the experiment are shown in Fig. 4A. In this case, $\dot{q}(r) = \epsilon I$, a product of ϵ, the absorption coefficient of PDA, and the laser irradiance at the location of the particle (I). In general, T is proportional to $\dot{q}$ (one can set $T = 0$ at the reference power) and depends on four parameters: r_c, r_p, κ_h, and κ_p. Two parameters, $\langle r_c \rangle \approx 55$ nm and $r_p \approx 113$ nm, have been obtained by analyzing TEM images (Fig. 1D) for the case of PDA synthesized using 500 μg/ml concentration of dopamine. The values of κ_p, the thermal conductivity of PDA, and $\dot{q}$ (assumed to be a constant within the PDA layer) should be determined before using PDA-FNDs for measuring the only remaining factor, the value of κ_h.

Although the main source of heat is absorption of the PDA shell, there is a small heating in the diamond core and/or on the diamond surface of the PDA-FND composite as indicated by the small upward trend shown in Fig. 2B for pristine FNDs. The measured value of the thermal conductivity will not be substantially affected by the diamond-related heat source, because this heat can be seen also as a result of an increased absorption of the PDA, which is an experimentally determined factor (see the Supplementary Materials). The temperature will still be highly uniform within the entire crystal due to the high thermal conductivity of diamond.

To determine κ_p and $\dot{q}$, temperature rises corresponding to the laser power increase from 7.3 to 25 mW were measured using different

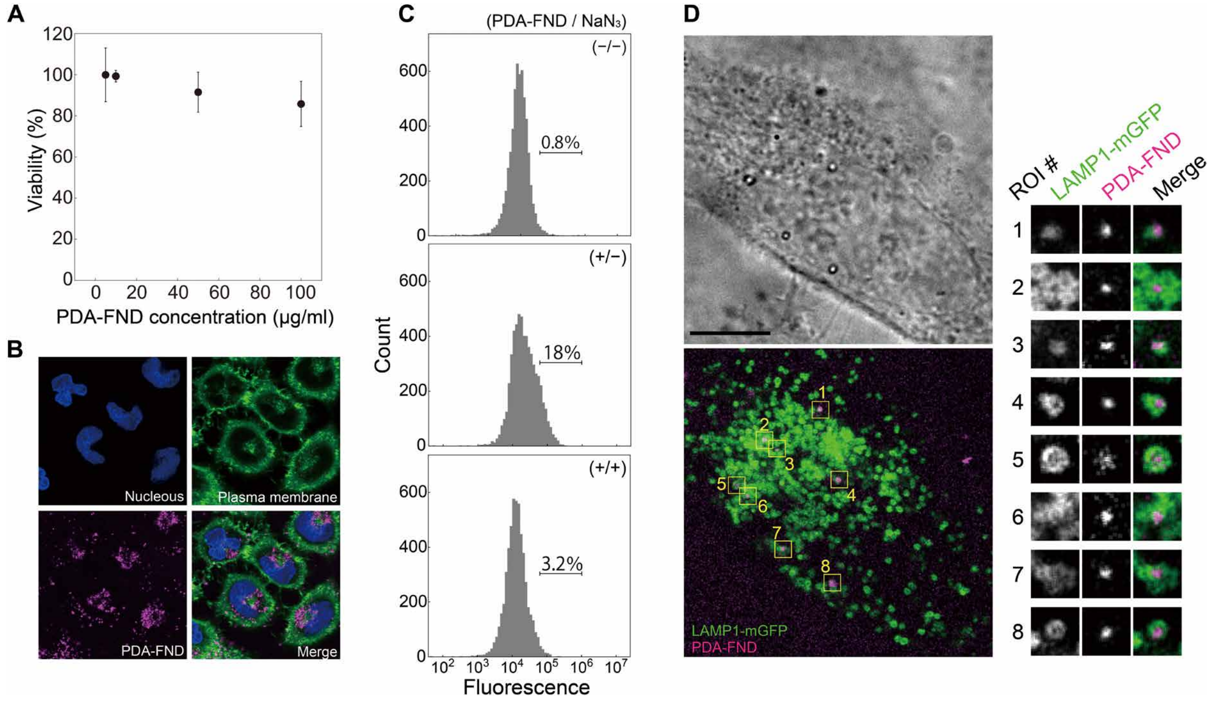

Fig. 3. Biocompatibility and subcellular localization of PDA-FNDs. (**A**) Cell viability test of HeLa cells treated with PDA-FNDs at various concentrations using the cell CCK-8 assay. The panel shows the corresponding mean values (circles) and the sample SDs (bars). (**B**) Confocal microscopic images of HeLa cells incubated with PDA-FNDs for 4 hours. Maximum of 10 confocal sections at the middle of cells overlaid. Image dimensions: 92 μm × 92 μm. (**C**) Flow cytometry cell sorting (FACS) analysis of the cellular uptake of PDA-FNDs with and without NaN_3 treatment. The range of highly fluorescent cells from 5×10^4 to 1×10^6 is indicated by the bar. The number on the bar represents the percentage of cells within the range. The fraction of cells within the range in non-treated HeLa cells (top) is about 0.8%. Loading with PDA-FNDs (middle) sharply elevates this fraction from 0.8 to 18%, implying the presence of cells containing PDA-FNDs. Loading with PDA-FNDs in the presence of 10 mM NaN_3 (bottom) results in the number within the range reduced to 3.2%. (**D**) Confocal microscopy images of HeLa cells overexpressing LAMP1-mGFP that were incubated with PDA-FNDs for 4 hours. Left: bright-field image showing a single optical section (top) and bottom fluorescence image showing the maximum intensity within 1.5 μm in depth (six confocal optical sections). Right: enlarged views of single optical sections from LAMP1-mGFP, PDA-FND, and their merges. Scale bar, 10 μm. ROI, region of interest.

PDA-FNDs in air, water, and oil as control media with known thermal conductivity values (*42–44*). ODMR spectra were obtained for PDA-FNDs attached to the bottom of the glass flow cell coated by polyethylenimine (PEI) with a thickness of 18 ± 5 nm (95% confidence interval estimated using 22 measurements) (fig. S7). The exact value of the thermal conductivity of PEI is not important because of its small thickness (table S1). The thermal conductivity of the glass substrate, $\kappa_{\mathrm{glass}} \sim 1.05\ \mathrm{W\ m^{-1}\ K^{-1}}$, is given in the literature (*45*).

The data, that is, the values of $dT_{7.3 \rightarrow 25}$ for a few tens of particles (ΔT_{m} for briefness) and the corresponding errors (σ_{m}) measured in the control media and cells, are shown as circles and error bars in Fig. 4B. In the analysis, we have assumed that the physical temperatures ΔT of these particles obey a normal distribution with a mean $\langle \Delta T \rangle$ and an SD $\sigma_{\Delta T}$. The possible reasons for the dispersion of data are, for example, distribution of FND diameters and/or difference in heat conductivity of the media surrounding each particle. The goal of the data analysis is to estimate the values of $\langle \Delta T \rangle$ and $\sigma_{\Delta T}$ and to determine the contributions of different factors to $\sigma_{\Delta T}$.

Bayesian analysis of the data is based on the theorem stating that conditional probability $P(\langle \Delta T \rangle, \sigma^2_{\Delta T}, \Delta T \mid D)$ is proportional to $P(D \mid \langle \Delta T \rangle, \sigma^2_{\Delta T}, \Delta T)$ and the prior $P(\langle \Delta T \rangle, \sigma^2_{\Delta T}, \Delta T)$. In this case, we assume

$$P(D \mid \langle \Delta T \rangle, \sigma^2_{\Delta T}, \Delta T) \propto \prod_m \exp\left(-\frac{(\Delta T - \Delta T_m)^2}{2\sigma^2_m}\right) \exp\left(-\frac{(\Delta T - \langle \Delta T \rangle)^2}{2\sigma^2_{\Delta T}}\right) \quad (2)$$

The posterior probabilities $P(\sigma^2_{\Delta T} \mid D)$ and $P(\langle \Delta T \rangle \mid D)$ are obtained by integrating out the other two variables in $P(\langle \Delta T \rangle, \sigma^2_{\Delta T}, \Delta T \mid D)$ as outlined in the Supplementary Materials.

Probability distributions $P(\langle \Delta T \rangle \mid D)$ are shown in Fig. 4C (left). The most probable values of $\langle \Delta T \rangle$ and their 95% confidence intervals are listed in Table 1. The two values κ_{p} and $\dot{q}$ were determined by numerical simulations. These values were tuned to obtain calculated temperatures $\langle \Delta T \rangle_{\mathrm{sim}}$, which best agree with the most probable values of $\langle \Delta T \rangle$ (Fig. 4D) in water, oil, and air. In these simulations, we have assumed that all media are homogeneous. It has been found that $\kappa_{\mathrm{p}} = 0.2\ \mathrm{W\ m^{-1}\ K^{-1}}$ and $\dot{q} = 80\ \mu\mathrm{W}\ \mu\mathrm{m}^{-3}$ reproduce within the accuracy of measurements of the corresponding measured values (Table 1). One may also determine κ_{p} and $\dot{q}$ using the most probable values of $\langle \Delta T \rangle$ for water and air only. Then, the thermal conductivity of oil κ_{oil} can be estimated as a fit parameter for matching $\langle \Delta T \rangle$ and $\langle \Delta T \rangle_{\mathrm{sim}}$ in oil. The value of $\kappa_{\mathrm{oil}} \approx 0.12\ \mathrm{W\ m^{-1}\ K^{-1}}$ obtained in such a way differs from the literature value by about 10% (table S2). The value of ϵ can be obtained using $\dot{q} = 80\ \mu\mathrm{W}\ \mu\mathrm{m}^{-3}$, the change of laser power in the experiment (≈18 mW), and the diameter of the illuminated area (≈40 μm). The estimated value $\epsilon \approx 5.6\ \mu\mathrm{m}^{-1}$ is in good agreement (given all the approximations made) with $3.7\ \mu\mathrm{m}^{-1}$ measured for a PDA film (*46*). These considerations validate our method of measurements.

The most probable mean value of the physical temperature rises $\langle \Delta T \rangle_{\mathrm{cell}}$ was 3.0 K in HeLa cells. The temperature rise of 3.0 K follows

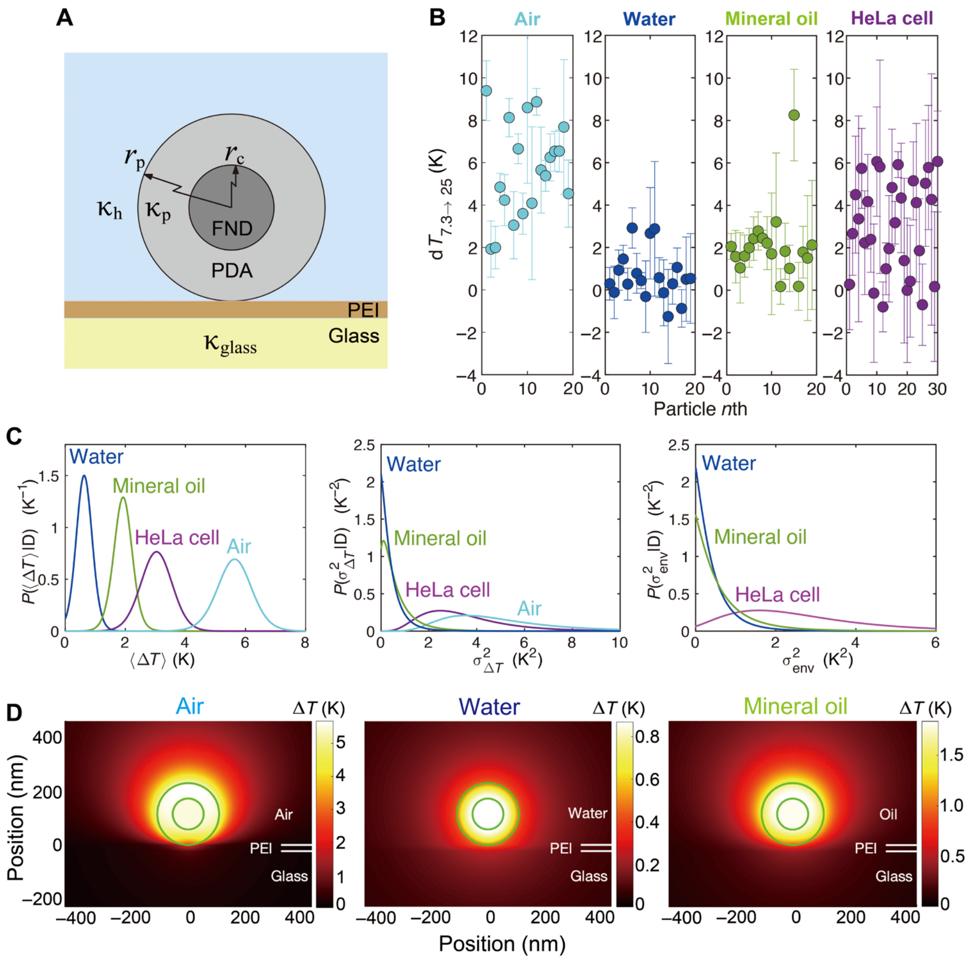

Fig. 4. In situ measurements of local thermal conductivity in air, water, mineral oil, and HeLa cells. (**A**) Model structure of a PDA-FND and its surroundings. The radius of the FND is r_c and the radius of the PDA-FND is r_p. The thermal conductivity of PDA is κ_p. The rest of the space is homogeneous, $\kappa = \kappa_h$. (**B**) Circles and error bars show $dT_{7.3\to 25}$ and their SDs measured for each particle in different environments. The values on the horizontal axes consecutively number PDA-FND particles used for measurements in each medium. (**C**) Posterior Bayesian inferences. From left to right: $P(\langle\Delta T\rangle \mid D)$ and $P(\sigma^2_{\Delta T} \mid D)$ (both for water, mineral oil, HeLa cell, and air); $P(\sigma^2_{env} \mid D)$ for water, oil, and cells. All the priors are uniform. (**D**) Numerical simulations of the temperature distributions in and around a PDA-FND in air, water, and mineral oil (from left to right) whose thermal conductivities are listed in Table 1. The thermal conductivity and the heat power density of PDA in all cases are 0.2 W m^{-1} K^{-1} and 80 μW μm^{-3}, respectively. A 20-nm-thick layer of polyethylenimine (PEI; thermal conductivity set as 0.2 W m^{-1} K^{-1}) is placed on the top of the glass substrate. Circles show the border lines of the FND (r_c = 55 nm) and the PDA shell (r_p = 110 nm). The diamond temperatures above the base temperature are listed in Table 1. Note the difference in the color scale.

Table 1. Values of $\langle\Delta T\rangle$ obtained experimentally and the corresponding results of numerical simulations in different media. Experimental errors represent 95% confidence intervals ($n \approx 20$ and 80 for batches 1 and 2, respectively). In all simulations, $\kappa_p = 0.2$ W m^{-1} K^{-1} and $\dot{q} = 80$ μW μm^{-3}. A 20-nm-thick layer of PEI ($\kappa_{PEI} = 0.2$ W m^{-1} K^{-1}) was placed on the top of the glass substrate (between the glass and the PDA-FNDs), while the whole assembly was immersed in air, water, or oil (as shown in Figure 4A). Inside cells, simulation has been performed without glass and PEI. The simulated values of ΔT and the derivatives in the last two columns were obtained using the shown values of κ_h.

Medium	**$\langle\Delta T\rangle$ (batch 1) (K)**	**$\langle\Delta T\rangle$ (batch 2) (K)**	**κ_h (literature) (W m^{-1} K^{-1})**	**ΔT (simulation) (K)**	**$\frac{\partial \Delta T}{\partial r_c}$ (K nm^{-1})**	**$\kappa_h^2 \frac{\partial \Delta T}{\partial \kappa_h}$ (W m^{-1})**
Air	5.6 ± 1.1	5.7 ± 0.8	0.026 (*42*)	5.32	0.070	−0.21
Water	0.63 ± 0.5	0.70 ± 0.3	0.61 (*43*)	0.84	0.0081	−0.15
Oil	1.9 ± 0.6	1.7 ± 0.4	0.135 (*44*)	1.76	0.021	−0.11
Cell	3.0 ± 1.0*	2.9 ± 0.8†	0.11 ± 0.04‡	3.00	0.040	−0.31

*HeLa. †MCF-7. ‡Current results.

from Eq. 1 if $\kappa_{\text{cell}} = 0.11 \pm 0.04$ W m^{-1} K^{-1}, while κ_{p} and $\dot{q}$ equal the values determined using the data for air, water, and oil. Note that, to avoid a cross-talk between PDA-FNDs, the concentration of PDA-FND solution applied to cells was reduced 20 times (to 0.5 μg/ml) compared to the amount used for studying intracellular localizations (cf. Fig. 3D). Very few or no PDA-FNDs were present in most of the cells. Numerical simulations show that the influence of the glass substrate on the FND temperature is negligible when the distance between the probe and the glass is larger than 200 nm (fig. S8), which is the case in cells. Analytical solution of the heat equation can be obtained for such a simplified geometry (Supplementary Materials and fig. S9). The exact analytical solution verifies the accuracy of the numerical calculations.

The posterior probability distributions $P(\sigma^2_{\Delta T} \mid D)$ are shown for all media in Fig. 4C (middle) and display clear maxima at about 3.6 and 2.5 K^2 in the case of air and cells, respectively. Assuming that ΔT is a function of r_{c} and κ_{h}, the variance $\sigma^2_{\Delta T}$ can be split in two parts as follows from the conventional error propagation

$$\sigma^2_{\Delta T} = \left(\frac{\partial \Delta T}{\partial r_{\text{c}}}\right)^2 \sigma^2_{r_{\text{c}}} + \left(\frac{\partial \Delta T}{\partial \kappa_{\text{h}}}\right)^2 \sigma^2_{\kappa_{\text{h}}} \qquad (3)$$

Because air is expected to be a homogeneous medium where $\sigma^2_{\kappa_{\text{h}}} = 0$, the value of $\sigma^2_{\Delta T} \approx 3.6$ K^2 and Eq. 3 can be used to conclude that $\sigma_{rc} \approx 27$ nm (see Table 1 for the value of the derivative). This value agrees with the estimate of $\sigma_{rc} \approx 24$ nm obtained from the TEM images (Fig. 1). Such agreement supports both the validity of the data analysis and the model. The value of σ_{rc} (it is the same in all media) and the derivative from Table 1 provide an estimate of the first term in Eq. 3 in cells. This estimate equals 0.9 K^2 (we use the more accurate value of σ_{rc} determined from TEM images) and is appreciably smaller than $\sigma^2_{\Delta T} = 2.5$ K^2. The difference of 1.6 K^2 points to a notable contribution of the second term in Eq. 3, which describes fluctuations of the local environment and will be referred to as σ^2_{env}. The distributions $P(\sigma^2_{\text{env}} \mid D)$ can be directly obtained from $P(\sigma^2_{\Delta T} \mid D)$ by subtracting $(\partial \Delta T / \partial r_{\text{c}})^2 \sigma^2_{r_{\text{c}}}$ from $\sigma^2_{\Delta T}$. These distributions for water, oil, and cell are shown in Fig. 4C (right). One can see that the peaks of $P(\sigma^2_{\text{env}} \mid D)$ are at zero in the case of water and oil as expected in media where it is reasonable to assume that $\sigma^2_{\text{env}} = 0$. However, the peak at $\sigma^2_{\text{env}} = 1.6$ K^2 in the case of cells indicates the likelihood that the thermal conductivity is not a constant value but depends on the location of the probe particle. The evaluation of the corresponding SD $\sigma_{\kappa\text{h}} \approx 0.04$ W K^{-1} m^{-1} (obtained using the derivative $\partial \Delta T / \partial \kappa_{\text{h}}$ given in Table 1) suggests that κ_{cell} may vary in the range (0.07 to 0.15) W K^{-1} m^{-1}. The width of the peak (the peak value is only a factor of 4.4 larger than the value at $\sigma^2_{\text{env}} = 0$) points toward a relatively large uncertainty in the above estimate of σ^2_{env}. Therefore, the variation and its origin should be subjected to scientific scrutiny in the future.

To provide additional support to the reliability of these results, we performed independent measurements in air, water, and oil environments along with MCF-7 cells ("batch 2," Table 1). The measurements of temperature rise obtained in the two completely independent experiments were very close to each other.

DISCUSSION

Intracellular thermal conductivity (κ_{cell}) is a key parameter characterizing heat transfer in living cells and has been experimentally determined here. Single-cell measurements of κ have been previously attempted by several researchers. Park *et al.* (*47*) reported a value similar to that of water based on a three-omega method, whereas the values for cancer cell lines determined by ElAfandy *et al.* (*48*) using nanomembranes were slightly less than those for water. These differences may be attributed to heat being supplied to the specimen from outside the cells. It is likely that κ was an average of the specimen including whole cells as well as extracellular matrices and nearby media. To determine the intracellular κ at a nanoscale level, both heating and temperature measurements should be confined to small volumes inside cells as we have demonstrated in the current study.

Bayesian analysis suggests that κ_{cell} is not a constant but can deviate from its average value. If one takes a minimal value of $\kappa_{\text{cell}} \approx 0.07$ W m^{-1}K^{-1}, then the steady-state $\Delta T \approx 1$ K (we set this value as a minimum temperature rise affecting biochemical processes) can be achieved in a spherical region generating 5 nW of heat power with a diameter of approximately 10 nm. While such a power is produced by rat brown adipocyte (*49*), the whole-cell power cannot be confined in a single hotspot. However, a significantly smaller than previously considered value of κ_{cell} partially closes the gap between calculations and measurements of the intracellular temperature heterogeneity. The remaining very large discrepancy of several orders of magnitude requires further consideration.

Much less power is needed to achieve a 1-K transient temperature rise. The heat conductivity, which is significantly smaller than the value previously assumed, reduces the speed with which the heat propagates through the intracellular medium. A transient value of ΔT in a region of radius a requires heat energy $E \approx 4\Delta T C a^3$, where C is the volumetric heat capacity. This temperature rise will last for the time interval $\tau \approx Ca^2/\kappa$ (*18*). If $a = 1$ μm, $\Delta T = 1$ K, $C = 4$ MJ m^{-3}K^{-1}, and $\kappa = 0.07$ W m^{-1} K^{-1}, then the required energy would be 16 pJ, approximately 10^{-3} times the energy of glucose, which is typically accumulated in a cell (*18*), while the corresponding $\tau \approx 60$ μs. Notably, this time scale is characteristic of the dynamics of some primary intracellular processes such as protein folding (*50*). Therefore, the new value of κ_{cell} makes biologically meaningful transient temperature rises in a cell much more feasible. This conclusion suggests that cells may use heat flux for short-distance thermal signaling.

The statistical variance of κ_{cell} may result from different conditions for heat transfer in the immediate vicinity of the PDA-FND particles. For example, although the majority of PDA-FNDs were found in LAMP1-GFP–positive vesicles, a small fraction of the particles was located either in the cytosol or in the LAMP1-GFP–negative vesicles as shown in Fig. 3D. In general, variation of the thermal conductivity is expected to increase with increasing spatial resolution of the measurements, because it is affected by the complex composition of the intracellular environment and high-density assemblages of various biomolecules in the cytosol and organelles.

Because the substrate has a negligible effect on the temperature of the particles imbedded in cells, one can analytically solve Eq. 1, assuming that PDA-FND is surrounded by a spherical shell of outer radius r_{i} (the thickness of the shell is then $r_{\text{i}} - r_{\text{p}}$) and thermal conductivity κ_{i} (see the Supplementary Materials). In this case, the temperature rise of the probe particle corresponds to an effective thermal conductivity κ_{eff} such that $1/\kappa_{\text{eff}}$ is a weighted average of $1/\kappa_{\text{h}}$ and $1/\kappa_{\text{i}}$

$$\frac{1}{\kappa_{\text{eff}}} \equiv \frac{r_{\text{p}}}{r_{\text{i}}}\frac{1}{\kappa_{\text{h}}} + \frac{r_{\text{i}} - r_{\text{p}}}{r_{\text{i}}}\frac{1}{\kappa_{\text{i}}} \qquad (4)$$

Thus, the measured value of thermal conductivity is between $1/\kappa_h$ and $1/\kappa_i$. For simplicity, we identify $\kappa_{cell} = \kappa_{eff}$, although, ultimately, a cell is characterized not by a single value but a three-dimensional map of thermal conductivity.

To identify the source of the κ_{cell} variations, it is necessary to accurately locate where the temperature is measured. Technical challenges should be overcome to achieve this. One approach could include using the catechol/quinone groups on the PDA as versatile platforms for functionalization (*31*) for the selective targeting of PDA-FNDs to biomolecules of interest and thus measuring thermal conductivity at specific intracellular organelles, for example, inside mitochondria.

The structure of PDA-FND is more uniform (Fig. 1) when compared to other hybrids with similar functions (*20*, *21*), but there remains notable heterogeneity among particles. Although the Bayesian statistical analysis of the results obtained in different media allows separation of the variance of the temperature rise caused by the inhomogeneity of κ_{cell} from the variance related to the heterogeneity of the particles, removing the latter factor would significantly increase the accuracy with which the value of κ_{cell} could be determined. Moreover, elimination of particle heterogeneity would enable single PDA-FND particle measurements of κ at specific locations. Since the production of physically and chemically uniform FNDs has yet to be achieved, we assume that PDA-FND heterogeneity is related to the intrinsic property of FNDs such as the size, shape, crystal strain, impurity content, and the number of NV^- centers. The problem caused by the heterogeneity of FNDs could be effectively mitigated if the same PDA-FND particles were used in different environments. As a proof of principle, a series of ODMR spectra were obtained for four PDA-FNDs attached to the bottom of a flow cell coated with PEI, while the flow cell that had been in air was filled sequentially with water and then oil (Supplementary Materials and fig. S10). Unfortunately, the effective delivery of a preselected particle into a cell is still an unresolved challenge.

In summary, we have successfully measured the intracellular thermal conductivity (κ_{cell}) of single living cells. The average κ_{cell} value is close to κ_{oil} and is one-sixth of κ_{water}. Further analyses suggested κ_{cell} variations due to significant differences in intracellular media. Our experimental results provide essential information for theoretical considerations of the role of heat transfer in cells. In particular, the hypothesis regarding heat-mediated intracellular signaling gains additional support and, perhaps, will result in a better understanding of the control and regulation processes of heat in living organisms at the single-cell level.

MATERIALS AND METHODS

Chemicals and materials

Dopamine hydrochloride (H8502-5G) and nocodazole (M1404-2MG) were purchased from Sigma-Aldrich Co. Ltd. (St. Louis, MO, USA). Tris (hydroxymethyl aminomethane) (35434-76) was purchased from Nacalai Tesque Inc. (Kyoto, Japan). Sodium azide (NaN_3) (195-11092) was purchased from FUJIFILM Wako Pure Chemical Corporation (Osaka, Japan). Hoechst 33342 (346-07951) and the cell counting kit-8 (CCK-8) (347-07621) were purchased from Dojindo Laboratories (Kumamoto, Japan). FNDs (BR100) were purchased from FND Biotech Inc. (Taipei, Taiwan). LAMP1-mGFP plasmid, which encodes a GFP-tagged lysosome marker, was a gift from E. Dell'Angelica (Addgene plasmid no. 34831; http://n2t.net/addgene:34831; RRID: Addgene_34831). Lipofectamine 3000 Transfection Kit (3000-015) was purchased from Invitrogen (Carlsbad, CA, USA). Dulbecco's modified Eagle's medium (DMEM) (11965-092), 0.25% trypsin-EDTA (25200-056), phosphate-buffered saline (PBS) (10010-023), penicillin and streptomycin (15140-122), fetal bovine serum (FBS) (10270-106), Alexa Fluor 488 *N*-hydroxysuccinimide (NHS) Ester (A20000), CellMask Green (C37608), ER-tracker (E34251), and Golgi tracker (B22650) were purchased from Thermo Fisher Scientific (Waltham, MA, USA).

Synthesis and characterization of PDA-FND particles

PDA-FNDs were prepared according to the protocol reported previously with minor modifications (*31*). To synthesize PDA-FND nanoparticles, 50 μg of FNDs was mixed with 1 ml of freshly prepared dopamine hydrochloride solutions at concentrations of 50, 300, and 500 μg/ml in 10 mM tris-HCl buffer (pH 8.5) and allowed to incubate for 16 hours under vigorous shaking at 298 K on a thermoshaker (TS-100C, Biosan Medical-biological Research and Technologies, Riga, Latvia). The resulting PDA-FNDs were collected by centrifugation at 3000*g* for 10 min at 298 K. Last, the nanoparticles were dispersed in Milli-Q water for further use. Dynamic light scattering and the zeta potentials of the nanoparticles were measured with a Malvern Zetasizer instrument (Zetasizer Nano ZSP, Malvern Instruments Limited, Worcestershire, UK). An H-7650 TEM (Hitachi High-Tech, Tokyo, Japan) operating at an accelerating voltage of 80 kV was adopted to characterize the size, PDA shell thickness, and structure of the FNDs and PDA-FNDs. The TEM samples were prepared by dropping 5 μl of solution onto 400-mesh carbon film–coated copper grids (24945-50, Polysciences Inc., Warrington, PA, USA), which were glow-discharged by a plasma cleaner. The grids were then air-dried and observed with the TEM.

TEM image analysis

ImageJ was used to analyze the TEM images of FNDs and PDA-FNDs. The FND radius was defined as half of the average length of horizontal and vertical lines drawn across the FND to pass through its center. To measure the thickness of the PDA layer, tangent lines were drawn at both ends of the vertical and horizontal lines. The lengths of the four-line segments, which were vertical to the tangent lines across the PDA layer, were measured. The thickness of the PDA layer was determined by averaging the four measurements.

Cell cultures and cytotoxicity assays with CCK-8

HeLa (American Type Culture Collection CCL-2) and MCF-7 (Japanese Collection of Research Bioresources JCRB0134) cells were seeded on 100-mm tissue culture dishes (TPP Techno Plastic Products AG, Switzerland) and were cultured in DMEM supplemented with 10% FBS, penicillin (100 IU/ml), and streptomycin (100 μg/ml) under a humidified atmosphere containing 5% CO_2.

To evaluate the cytotoxicity of PDA-FNDs, HeLa cells were seeded into 96-well plates (Thermo Fisher Scientific, Waltham, MA, USA) at a density of 5000 per well. After 24 hours, the cells were treated with PDA-FNDs at various concentrations and incubated for 4 hours at 310 K. The residual PDA-FNDs were then removed by washing, and the samples were incubated overnight at 310 K. The next day, cell viability was determined using a microplate reader (Thermo Scientific Multiskan FC, Thermo Fisher Scientific Oy, Ratstie, Finland) according to the CCK-8 manufacturer's protocol. Water-soluble tetrazolium salt [WST-8; 2-(2-methoxy-4-nitrophenyl)-3-(4-nitrophenyl)-5-(2,4-disulfophenyl)-2*H*-tetrazolium] is reduced by cellular dehydrogenase activity to yield a yellow-colored formazan dye. The 450-nm absorption before the addition of the CCK-8 solution was deducted to subtract the absorption of PDA-FNDs inside the HeLa cells. The viability of HeLa cells treated with PDA-FNDs was expressed as a percentage of the viability of HeLa cells grown in the absence of PDA-FNDs.

Fluorescent staining of subcellular organelles and confocal fluorescence microscopy

HeLa cells were seeded in 35-mm glass-based dishes (IWAKI, Shizuoka, Japan). PDA-FNDs were dispersed in culture medium and were applied to HeLa cells. After a 4-hour incubation at 310 K, the cells were stained with CellMask Green Plasma Membrane Stain (excitation: 522 nm and emission: 535 nm) (1:2000 dilution) and Hoechst 33342 (1 μg/ml; 355 and 461 nm) to visualize the plasma membrane and nucleus, respectively, according to the manufacturer's procedures. Cells were also stained for ER with 500 nM ER-tracker Green (504 and 511 nm), for Golgi apparatus with 250 nM BODIPY FL C_5-ceramide complexed to bovine serum albumin (505 and 511 nm), and for mitochondria with 5 μM MitoTracker Green FM (490 and 516 nm) to examine colocalizations with these intracellular organelles. To inhibit the energy-dependent process of endocytosis, HeLa cells were treated with 10 mM NaN_3 for 30 min. The cells were then incubated with PDA-FNDs for 4 hours, followed by CellMask Green staining, and the prepared specimens were observed using a Leica TCS SP8 confocal microscope (Leica Microsystems, Germany) with a 63× objective lens (HC PL APO CS2 63×/1.40 OIL). Images are smoothed, and the brightness and the contrast were adjusted for viewing purpose.

Fluorescence-activated cell sorting

HeLa cells were seeded into a 96-well plate, and PDA-FNDs were added to the cells once they reached confluency. After a 4-hour incubation at 310 K, unbound PDA-FNDs were removed by washing, and the cells were collected by centrifugation at 140*g* following trypsin-EDTA treatment. The cell pellet was washed twice in PBS and resuspended in 100 μl of PBS. The samples were then subjected to FACS analysis at an excitation of 561 nm and an emission of 675 to 715 nm using an Attune NxT Flow Cytometer (Thermo Fisher Scientific). For the NaN_3 treatment group, HeLa cells were pretreated with 10 mM NaN_3 for 30 min before loading the PDA-FNDs, and 10 mM NaN_3 was present in all the solutions during the incubations, sample collections, and measurements.

Overexpression of LAMP1-mGFP in HeLa cells

HeLa cells were transfected with a LAMP1-mGFP plasmid by using a Lipofectamine 3000 Transfection Kit. After 24 hours, the cells were loaded with PDA-FNDs (10 μg/ml) and incubated at 310 K for 4 hours. The unbound PDA-FNDs were removed by washing, and the cells were incubated overnight and visualized using a fluorescence confocal microscope (Leica Microsystems, Germany).

Temperature measurements using FNDs through ODMR microscopy

Temperatures were measured using FNDs and a homebuilt microscope, which was reported previously (*25*, *33*). Briefly, a continuous neodymium-doped yttrium aluminum garnet (Nd:YAG) laser at 532 nm illuminated FNDs in PDA-FND nanoparticles to initialize and read out the spin state of NVCs on an inverted microscope system (Nikon, Ti-E). Fluorescence from the NVCs was captured by an oil immersion objective lens (Nikon SR HP Apo TIRF, 100×, numerical aperture 1.49), passed through a long-pass filter to cut off the excitation light, and imaged by an electron-multiplying charge-coupled device camera (EMCCD; Andor, iXon 860). A two-turn copper coil with a diameter of approximately 1 mm was placed just above the coverslip to irradiate the sample with MWs at frequencies near the electron spin resonance in NVCs. A gate pulse provided by a pulser (Berkeley Nucleonics Corporation, 565) activated an MW generator (Agilent, E8257D) to output an MW pulse, which was then amplified by linear MW power amplifiers (Mini Circuits, PAN35-5A and ZHL-16W-43+) and transmitted through a coaxial cable to the MW coil. The pulser and the image acquisition by the EMCCD camera were synchronized using a computer (Dell T3500, XT, USA) with LabVIEW software (National Instruments, TX, USA). ODMR spectra were recorded for a range of MW frequencies as the difference between the fluorescence intensities with and without MW irradiation. The temperature of the sample was set at 300 K by a stage-top incubator (Tokai Hit, TPi-108RH26) on a motorized stage.

Evaluation of the photothermal effect of PDA-FNDs

Glass-based dishes were first coated with a thin layer of positively charged PEI to improve the adhesion of negatively charged PDA-FNDs (fig. S1), and then PDA-FNDs were scattered on the dish. Fluorescence images were recorded while the MW frequency was digitally swept across the range from 2860 to 2978 MHz at increments of 0.18 MHz. The exposure time of the EMCCD camera was altered from 0.05 to 0.005 s depending on the laser intensity. A set of images (two for cell experiments and 64 for other cases) were accumulated per MW frequency, and two scans (32 for cell experiments) were performed. Through this process, ODMR spectra were obtained from isolated PDA-FND particles located in the field of view. Each spectrum was fitted to the six-parameter superposition of two Lorentzian functions

$$R = 1 - \frac{A_1}{1 + (\omega - D_{gs} + E)^2/\Gamma_1^2} - \frac{A_2}{1 + (\omega - D_{gs} - E)^2/\Gamma_2^2} \quad (5)$$

where the MW frequency ω assumes a discrete set of values ω_n incremented at 0.18 MHz. The χ^2 function of six parameters in Eq. 5 is defined as

$$\chi^2 \equiv \sum_n \left[1 - \frac{A_1}{1 + (\omega_n - D_{gs} + E)^2/\Gamma_1^2} - \frac{A_2}{1 + (\omega_n - D_{gs} - E)^2/\Gamma_2^2} - \frac{L(\omega_n)}{L_0(\omega_n)}\right]^2 \quad (6)$$

where $L(\omega_n)$ and $L_0(\omega_n)$ are the measured luminescence intensities with MW power "on" and "off," respectively. The minimum of χ^2 was found numerically for each measured ODMR spectrum. The corresponding values of all parameters are their best posterior estimates. The second derivatives of χ^2 at the minimum were used to estimate the covariance matrix whose diagonal elements are the variances for each parameter in Eq. 5 and they define the precision for each fitted parameter.

The temperature change in each FND was determined relative to the temperature at a reference excitation laser power, which was either 7.3 or 0.95 mW. For example, $dT_{7.3\rightarrow P} = \gamma\Delta D_{gs}$, where ΔD_{gs} is the change of D_{gs} when the laser power changes from 7.3 mW to P.

Numerical simulations

Numerical solutions of Eq. 1 have been obtained using PDE Modeler, an interactive MATLAB toolbox for solving partial differential equations in two dimensions. The toolbox helps in setting the boundary conditions and semi-automatically generates a variable mesh spacing. We have exploited cylindrical symmetry of the geometry in Fig. 4A, which allows for treating a three-dimensional problem as effectively two-dimensional in cylindrical coordinates. The temperature at the boundary of the cylindrical region has been fixed at zero. The solutions have been obtained in a region with a diameter of 16 μm and a height of 16 μm. The dimensions are chosen so that the temperature in the center of the PDA-FND particle decreases by less than 0.01 K if the size is reduced by a factor of 2. The mesh spacing has been selected so that increasing the spacing by a factor of 4 results in a less than 0.01 K temperature change of the PDA-FND particle.

ODMR measurement of PDA-FNDs inside HeLa or MCF-7 cells

HeLa or MCF-7 cells were cultured on 35-mm glass-based dishes and incubated with PDA-FNDs (0.5 μg/ml) for 4 hours. Unbound PDA-FNDs were then removed by washing, and the cells were cultured at 310 K overnight. The cells were then washed once with serum-free DMEM, and the medium was replaced with 2 ml of 10 μM nocodazole dissolved in phenol red–free DMEM. After a 30-min incubation at 310 K, ODMR measurements of the cells in interphase were performed.

Measurements of the thickness of the PEI layer using high-speed AFM combined with fluorescence microscopy

PEI solution containing Alexa Fluor 488 NHS Ester (10 μg/ml; Alexa488-PEI) was applied to a glass coverslip to prepare the PEI layer. First, the coverslip was observed under a fluorescence microscope to identify the edges of the Alexa488-PEI layer. A part of the coverslip containing the edge of the Alexa488-PEI layer was cut into an approximately 2-mm square fragment. The fragment was glued onto the AFM sample stage. Then, measurements of the thickness of the Alexa488-PEI layer were performed with a laboratory-built high-speed AFM (HS-AFM) apparatus. The HS-AFM is similar to the HS-AFM previously reported (*51*, *52*), whereas the current apparatus was customized to capture a fluorescence image of the sample on the AFM stage. The HS-AFM was equipped with small cantilevers [$k = 0.1$ to 0.2 N/m, $f = 800$ to 1200 kHz in water (Olympus)] and operated in tapping mode. The cantilever was maneuvered onto the edge of the Alexa488-PEI layer with the guidance of the AFM fluorescence image. HS-AFM observations were performed under ultrapure water at 298 K. The height of the Alexa488-PEI layer in the AFM images was analyzed using IGOR Pro (WaveMetrics).

SUPPLEMENTARY MATERIALS

Supplementary material for this article is available at http://advances.sciencemag.org/cgi/content/full/7/3/eabd7888/DC1

View/request a protocol for this paper from *Bio-protocol*.

REFERENCES AND NOTES

1. J. M. Grady, B. J. Enquist, E. Dettweiler-Robinson, N. A. Wright, F. A. Smith, Evidence for mesothermy in dinosaurs. *Science* **344**, 1268–1272 (2014).
2. B. J. D. Meeuse, I. Raskin, Sexual reproduction in the arum lily family, with emphasis on thermogenicity. *Sex. Plant Reprod.* **1**, 3–15 (1988).
3. I. Terry, G. H. Walter, C. Moore, R. Roemer, C. Hull, Odor-mediated push-pull pollination in cycads. *Science* **318**, 70 (2007).
4. N. C. Wegner, O. E. Snodgrass, H. Dewar, J. R. Hyde, Whole-body endothermy in a mesopelagic fish, the opah, lampris guttatus. *Science* **348**, 786–789 (2015).
5. G. Newport, On the temperature of insects, and its connexion with the functions of respiration and circulation in this class of invertebrated animals. *Phil. Trans. R. Soc. A* **127**, 259–338 (1837).
6. B. Heinrich, Why have some animals evolved to regulate a high body temperature? *Am. Nat.* **111**, 623–640 (1977).
7. M. Quintanilla, L. M. Liz-Marzán, Guiding rules for selecting a nanothermometer. *Nano Today* **19**, 126–145 (2018).
8. C. D. S. Brites, P. P. Lima, N. J. O. Silva, A. Millán, V. S. Amaral, F. Palacio, L. D. Carlos, Thermometry at the nanoscale. *Nanoscale* **4**, 4799–4829 (2012).
9. K. Okabe, N. Inada, C. Gota, Y. Harada, T. Funatsu, S. Uchiyama, Intracellular temperature mapping with a fluorescent polymeric thermometer and fluorescence lifetime imaging microscopy. *Nat. Commun.* **3**, 705 (2012).
10. S. Kiyonaka, T. Kajimoto, R. Sakaguchi, D. Shinmi, M. Omatsu-Kanbe, H. Matsuura, H. Imamura, T. Yoshizaki, I. Hamachi, T. Morii, Y. Mori, Genetically encoded fluorescent thermosensors visualize subcellular thermoregulation in living cells. *Nat. Methods* **10**, 1232–1238 (2013).
11. K. Okabe, R. Sakaguchi, B. Shi, S. Kiyonaka, Intracellular thermometry with fluorescent sensors for thermal biology. *Pflugers Arch.* **470**, 717–731 (2018).
12. D. Chrétien, P. Bénit, H. Ha, S. Keipert, R. El-Khoury, Y. Chang, M. Jastroch, H. T. Jacobs, P. Rustin, M. Rak, Mitochondria are physiologically maintained at close to 50°C. *PLoS Biol.* **16**, e2003992 (2018).
13. G. Baffou, H. Rigneault, D. Marguet, L. Jullien, A critique of methods for temperature imaging in single cells. *Nat. Methods* **11**, 899–901 (2014).
14. S. Kiyonaka, R. Sakaguchi, I. Hamachi, T. Morii, T. Yoshizaki, Y. Mori, Validating subcellular thermal changes revealed by fluorescent thermosensors. *Nat. Methods* **12**, 801–802 (2015).
15. M. Suzuki, V. Zeeb, S. Arai, K. Oyama, S. Ishiwata, The 10^5 gap issue between calculation and measurement in single-cell thermometry. *Nat. Methods* **12**, 802–803 (2015).
16. G. Baffou, H. Rigneault, D. Marguet, L. Jullien, Reply to: "Validating subcellular thermal changes revealed by fluorescent thermosensors" and "The 10^5 gap issue between calculation and measurement in single-cell thermometry". *Nat. Methods* **12**, 803 (2015).
17. S. Uchiyama, C. Gota, T. Tsuji, N. Inada, Intracellular temperature measurements with fluorescent polymeric thermometers. *Chem. Commun. (Camb.)* **53**, 10976–10992 (2017).
18. M. Suzuki, T. Plakhotnik, The challenge of intracellular temperature. *Biophys. Rev.* **12**, 593–600 (2020).
19. A. R. N. Bastos, C. D. S. Brites, P. A. Rojas-Gutierrez, C. DeWolf, R. A. S. Ferreira, J. A. Capobianco, L. D. Carlos, Thermal properties of lipid bilayers determined using upconversion nanothermometry. *Adv. Funct. Mater.* **29**, 1905474 (2019).
20. P. C. Tsai, O. Y. Chen, Y. K. Tzeng, Y. Y. Hui, J. Y. Guo, C. C. Wu, M. S. Chang, H. C. Chang, Gold/diamond nanohybrids for quantum sensing applications. *EPJ Quantum Technol.* **2**, 19 (2015).
21. P. C. Tsai, C. P. Epperla, J. S. Huang, O. Y. Chen, C. C. Wu, H. C. Chang, Measuring nanoscale thermostability of cell membranes with single gold-diamond nanohybrids. *Angew. Chem. Int. Ed. Eng.* **56**, 3025–3030 (2017).
22. S. J. Yu, M. W. Kang, H. C. Chang, K. M. Chen, Y. C. Yu, Bright fluorescent nanodiamonds: No photobleaching and low cytotoxicity. *J. Am. Chem. Soc.* **127**, 17604–17605 (2005).
23. C. C. Fu, H. Y. Lee, K. Chen, T. S. Lim, H. Y. Wu, P. K. Lin, P. K. Wei, P. H. Tsao, H. C. Chang, W. Fann, Characterization and application of single fluorescent nanodiamonds as cellular biomarkers. *Proc. Natl. Acad. Sci. U.S.A.* **104**, 727–732 (2007).
24. G. Kucsko, P. C. Maurer, N. Y. Yao, M. Kubo, H. J. Noh, P. K. Lo, H. Park, M. D. Lukin, Nanometre-scale thermometry in a living cell. *Nature* **500**, 54–58 (2013).
25. S. Sotoma, C. P. Epperla, H. C. Chang, Diamond nanothermometry. *ChemNanoMat* **4**, 15–27 (2018).
26. J. Choi, H. Zhou, R. Landig, H. Y. Wu, X. Yu, S. V. Stetina, G. Kucsko, S. Mango, D. Needleman, A. D. T. Samuel, P. Maurer, H. Park, M. D. Lukin, Probing and manipulating embryogenesis via nanoscale thermometry and temperature control. *Proc. Natl. Acad. Sci. U.S.A.* **117**, 14636–14641 (2020).
27. L. Tong, Y. Zhao, T. B. Huff, M. N. Hansen, A. Wei, J. X. Cheng, Gold nanorods mediate tumor cell death by compromising membrane integrity. *Adv. Mater.* **19**, 3136–3141 (2007).
28. H. Lee, S. M. Dellatore, W. M. Miller, P. B. Messersmith, Mussel-inspired surface chemistry for multifunctional coatings. *Science* **318**, 426–430 (2007).
29. B. Poinard, S. Z. Y. Neo, E. L. L. Yeo, H. P. S. Heng, K. G. Neoh, J. C. Y. Kah, Polydopamine nanoparticles enhance drug release for combined photodynamic and photothermal therapy. *ACS Appl. Mater. Interfaces* **10**, 21125–21136 (2018).
30. Y. Zeng, W. Liu, Z. Wang, S. Singamaneni, R. Wang, Multifunctional surface modification of nanodiamonds based on dopamine polymerization. *Langmuir* **34**, 4036–4042 (2018).

31. H. S. Jung, K. J. Cho, Y. Seol, Y. Takagi, A. Dittmore, P. A. Roche, K. C. Neuman, Polydopamine encapsulation of fluorescent nanodiamonds for biomedical applications. *Adv. Funct. Mater.* **28**, 1801252 (2018).
32. Y. Liu, K. Ai, J. Liu, M. Deng, Y. He, L. Lu, Dopamine-melanin colloidal nanospheres: An efficient near-infrared photothermal therapeutic agent for in vivo cancer therapy. *Adv. Mater.* **25**, 1353–1359 (2013).
33. T. Sekiguchi, S. Sotoma, Y. Harada, Fluorescent nanodiamonds as a robust temperature sensor inside a single cell. *Biophys. Physicobiol.* **15**, 229–234 (2018).
34. V. M. Acosta, E. Bauch, M. P. Ledbetter, A. Waxman, L. S. Bouchard, D. Budker, Temperature dependence of the nitrogen-vacancy magnetic resonance in diamond. *Phys. Rev. Lett.* **104**, 070801 (2010).
35. Z. Xia, Z. Lin, Y. Xiao, L. Wang, J. Zheng, H. Yang, G. Chen, Facile synthesis of polydopamine-coated molecularly imprinted silica nanoparticles for protein recognition and separation. *Biosens. Bioelectron.* **47**, 120–126 (2013).
36. Q. Zheng, T. Lin, H. Wu, L. Guo, P. Ye, Y. Hao, Q. Guo, J. Jiang, F. Fu, G. Chen, Mussel-inspired polydopamine coated mesoporous silica nanoparticles as pH-sensitive nanocarriers for controlled release. *Int. J. Pharm.* **463**, 22–26 (2014).
37. V. Vaijayanthimala, Y. K. Tzeng, H. C. Chang, C. L. Li, The biocompatibility of fluorescent nanodiamonds and their mechanism of cellular uptake. *Nanotechnology* **20**, 425103 (2009).
38. K. Turcheniuk, V. N. Mochalin, Biomedical applications of nanodiamond (review). *Nanotechnology* **28**, 252001 (2017).
39. X. Liu, J. Cao, H. Li, J. Li, Q. Jin, K. Ren, J. Ji, Mussel-inspired polydopamine: A biocompatible and ultrastable coating for nanoparticles in vivo. *ACS Nano* **7**, 9384–9395 (2013).
40. S. Mukherjee, R. N. Ghosh, F. R. Maxfield, Endocytosis. *Physiol. Rev.* **77**, 759–803 (1997).
41. J. M. Falcon-Perez, R. Nazarian, C. Sabatti, E. C. Dell'Angelica, Distribution and dynamics of Lamp1-containing endocytic organelles in fibroblasts deficient in BLOC-3. *J. Cell Sci.* **118**, 5243–5255 (2005).
42. K. Kadoya, N. Matsunaga, A. Nagashima, Viscosity and thermal conductivity of dry air in the gaseous phase. *J. Phys. Chem. Ref. Data Monogr.* **14**, 947–970 (1985).
43. M. L. V. Ramires, C. A. Nieto de Castro, Y. Nagasaka, A. Nagashima, M. J. Assael, W. A. Wakeham, Standard reference data for the thermal conductivity of water. *Phys. Chem. Ref. Data* **24**, 1377–1381 (1995).
44. Z. Nadolny, G. Dombek, P. Przybylek, Thermal properties of a mixture of mineral oil and synthetic ester in terms of its application in the transformer, in *Proceedings of the IEEE Conference on Electrical Insulation and Dielectric Phenomena* (*CEIDP*) (2016).
45. M. J. Assael, S. Botsios, K. Gialou, I. N. Metaxa, Thermal conductivity of polymethyl methacrylate (PMMA) and borosilicate crown glass BK7. *Int. J. Thermophys.* **26**, 1595–1605 (2005).
46. V. Ball, Determination of the extinction coefficient of "polydopamine" films obtained by using $NaIO_4$ as the oxidant. *Mater. Chem. Phys.* **186**, 546–551 (2017).
47. B. K. Park, N. Yi, J. Park, D. Kim, Thermal conductivity of single biological cells and relation with cell viability. *Appl. Phys. Lett.* **102**, 203702 (2013).
48. R. T. ElAfandy, A. F. AbuElela, P. Mishra, B. Janjua, H. M. Oubei, U. Büttner, M. A. Majid, T. K. Ng, J. S. Merzaban, B. S. Ooi, Nanomembrane-based, thermal-transport biosensor for living cells. *Small* **13**, 1603080 (2017).
49. D. G. Clark, M. Brinkman, S. D. Neville, Microcalorimetric measurements of heat production in brown adipocytes from control and cafeteria-fed rats. *Biochem. J.* **235**, 337–342 (1986).
50. J. Kubelka, J. Hofrichter, W. A. Eaton, The protein folding "speed limit". *Curr. Opin. Struct. Biol.* **14**, 76–88 (2004).
51. T. Uchihashi, N. Kodera, T. Ando, Guide to video recording of structure dynamics and dynamic processes of proteins by high-speed atomic force microscopy. *Nat. Protoc.* **7**, 1193–1206 (2012).
52. H. Yamashita, K. Inoue, M. Shibata, T. Uchihashi, J. Sasaki, H. Kandori, T. Ando, Role of trimer-trimer interaction of bacteriorhodopsin studied by optical spectroscopy and high-speed atomic force microscopy. *J. Struct. Biol.* **184**, 2–11 (2013).
53. N. B. Manson, J. P. Harrison, Photo-ionization of the nitrogen-vacancy center in diamond. *Diam. Relat. Mater.* **14**, 1705–1710 (2005).

Acknowledgments: We thank Y. Yoshinari for preparing the ODMR microscope and F. Sugihara for technical advice on FACS. We also thank S. Ishiwata for valuable comments and discussion. **Funding:** This work was supported by Grant-in-Aid for JSPS Research Fellow A18J002870 (to S.S.), by Early-Career Scientists 19K16089 (to S.S.), by ATI Research Grant RG3004 (to S.S.), by JSPS KAKENHI JP15H05931 and JP18H01838 (both to Y.H.) and JP15K05251 and JP16KK0105 (both to M.S.), by the Japan Science and Technology Agency JPMJPR15F5 (to M.S.) and JPMJPR15FD (to H.Y.), by the Human Frontier Science Program RGP0047/2018 (to T.P. and M.S.), by Kurita Water and Environment Foundation 17D002 (to M.S.), and by Iketani Science and Technology Foundation 0301009-A (to M.S.). **Author contributions:** S.S., C.Z., J.C.Y.K., T.P., Y.H., and M.S. designed the experiments. S.S. and C.Z. synthesized and characterized the PDA-FNDs. C.Z. performed the cell viability tests and intracellular localization analyses. S.S. performed the ODMR measurements. H.Y. performed the HS-AFM measurements. T.P. performed the theoretical studies and numerical simulations. S.S., C.Z., H.Y., T.P., and M.S. analyzed the data. S.S., C.Z., H.Y., T.P., Y.H., and M.S. wrote the paper with input from J.C.Y.K. **Competing interests**: The authors declare that they have no competing interests. **Data and materials availability:** All data needed to evaluate the conclusions in the paper are present in the paper and/or the Supplementary Materials. Additional data related to this paper may be requested from the authors.

Submitted 14 July 2020
Accepted 30 November 2020
Published 15 January 2021
10.1126/sciadv.abd7888

Citation: S. Sotoma, C. Zhong, J. C. Y. Kah, H. Yamashita, T. Plakhotnik, Y. Harada, M. Suzuki, In situ measurements of intracellular thermal conductivity using heater-thermometer hybrid diamond nanosensors. *Sci. Adv.* **7**, eabd7888 (2021).